



CHORUS

This is the accepted manuscript made available via CHORUS. The article has been published as:

Mode-coupling mechanisms in nanocontact spin-torque oscillators

Ezio Iacocca, Philipp Dürrenfeld, Olle Heinonen, Johan Åkerman, and Randy K. Dumas
Phys. Rev. B **91**, 104405 — Published 11 March 2015

DOI: [10.1103/PhysRevB.91.104405](https://doi.org/10.1103/PhysRevB.91.104405)

Mode coupling mechanisms in nanocontact spin torque oscillators

Ezio Iacocca,^{1,2} Philipp Dürrenfeld,¹ Olle Heinonen,^{3,4} Johan Åkerman,^{1,2,5} and Randy K. Dumas^{1,2}

¹*Physics Department, University of Gothenburg, 412 96, Gothenburg, Sweden*

²*NanOsc AB, 16440 Kista, Sweden*

³*Materials Science Division, Argonne National Laboratory, Lemont, IL 60439, USA*

⁴*Northwestern-Argonne Institute for Science and Engineering, Evanston, IL 60208, USA*

⁵*Material Physics, School of ICT, Royal Institute of Technology, Electrum 229, 164 40, Kista, Sweden*

Spin torque oscillators (STOs) are devices that allow for the excitation of a variety of magneto-dynamical modes at the nanoscale. Depending on both external conditions and intrinsic magnetic properties, STOs can exhibit regimes of mode-hopping and even mode coexistence. Whereas mode-hopping has been extensively studied in STOs patterned as nanopillars, coexistence has been only recently observed for localized modes in nanocontact STOs (NC-STOs) where the current is confined to flow through a NC fabricated on an extended pseudo spin valve. By means of electrical characterization and a multi-mode STO theory, we investigate the physical origin of the mode coupling mechanisms favoring coexistence. Two coupling mechanisms are identified: *(i)* magnon mediated scattering and *(ii)* inter-mode interactions. These mechanisms can be physically disentangled by fabricating devices where the NCs have an *elliptical cross-section*. The generation power and linewidth from such devices are found to be in good qualitative agreement with the theoretical predictions, as well as provide evidence of the dominant mode coupling mechanisms.

I. INTRODUCTION

Spin torque oscillators (STOs)^{1,2} are devices in which magnetization dynamics in a thin film ferromagnet can be excited by means of the spin transfer torque (STT) effect^{3,4}. Depending on the geometry and magnetic properties of the free layer, propagating spin waves (SWs)⁵⁻⁷, solitonic modes⁸⁻¹¹, vortex gyration^{12,13}, and magnetic dissipative droplets¹⁴⁻¹⁷ have been observed. STOs can also be used to generate SWs in physically extended thin films, which is of particular interest for future magnonic applications^{18,19}. To date the generation of SWs using STT into extended films have been achieved in two types of structures: the spin Hall nano-oscillator, where the current is confined by patterning Au needles^{20,21} and the spin polarization provided by the spin Hall effect²² and in nanocontact spin torque oscillators (NC-STOs)¹ where the current is confined by patterning a metallic NC on top of an extended spin valve.

NC-STOs with permalloy free layers exhibit a particularly rich and reproducible dynamical phase space, featuring a transition between a propagating mode and two localized modes depending only on the out-of-plane external magnetic field angle, θ . The effect of the current-induced Oersted field, H_{Oe} , has been recently shown to be critical in determining the SW propagation direction and mode volume^{11,23}. Moreover, the energy landscape induced by the Oersted field was shown to determine the position of the localized modes^{11,24}. Such localization can be observed from micromagnetic simulations by calculating the mode energy distribution, or the spatial representation of the power spectral density, shown in Fig. 1(a-b), where black indicates zero power and light yellow indicates the (scaled) maximum power. In particular, a low frequency mode, identified as a spin wave bullet^{8,10}, is primarily located at the local field minimum (B) while a high frequency mode is primarily located at

the local field maximum (HF). This situation can also be schematically represented by the frequency landscape along $X = 0$, Fig. 1(c). Additionally, such a spatial localization was shown to promote mode coexistence in these devices¹¹. In a recent multi-mode theory developed for STOs²⁵⁻²⁸, a coexistence regime was found to be favored by mode coupling. However, both the experimental and theoretical studies to date emphasize the mode-hopping regime, *i.e.*, when only one mode exists at a particular instance of time. Consequently, the physical origin and coupling mechanisms behind mode coexistence are not well understood. To elucidate the characteristics of, and conditions for, mode coexistence we study NC-STOs devices specifically tailored to test the predictions of the multi-mode theory for STOs.

In this paper, we derive an expression for the generation linewidth of a multi-mode STO, in particular for the case of coexisting modes of generally different frequencies. We identify two mode coupling mechanisms: *(i)* magnon mediated scattering, originating from the interaction between the dominant modes and a bath of thermally excited magnons; and *(ii)* inter-mode exchange, originating from the non-local dipole or exchange coupling between the dominant, finite-volume modes. The resulting linewidth is found to have a very different dependence on these mode-coupling mechanisms. To test our theoretical predictions, NC-STOs were fabricated with elliptical NCs that break the symmetry and thus disentangle the mode-coupling mechanisms. The electrical characterization of these devices provides evidence for the underlying mode-coupling mechanisms and their effects on the magnetodynamics. Furthermore, these NC-STOs represent a model system to understand the effects of multi-mode generation and coupling, and allow one to propose novel methods to further tune the magnetodynamics at the nanoscale. In particular, the coupling between well-defined modes can play a fundamental role in

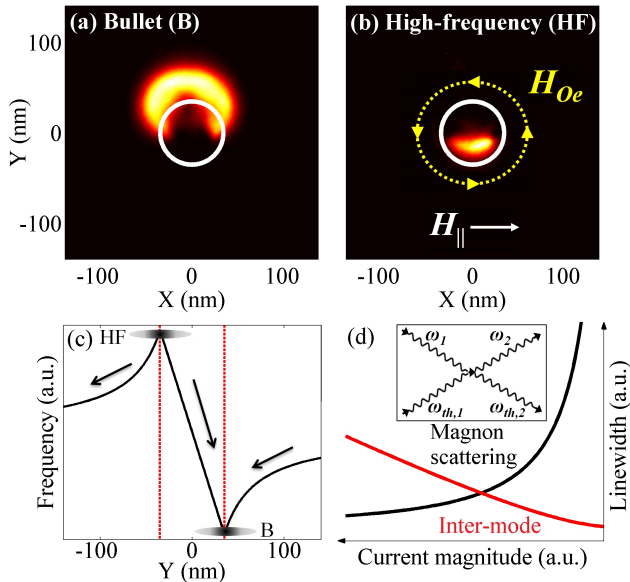


FIG. 1. (Color online) Mode energy distribution for the bullet (a) and high frequency (b) modes for a NC-STO with a circular NC. The relative orientation of the current-induced Oersted field (yellow) and in-plane applied field component (white) are indicated in (b). (c) Schematic representation of the local frequency landscape along the Y -direction in a NC-STO modified by the current-induced Oersted field (black line). The red dashed lines indicate the edges of the NC. The bullet mode, B (high frequency mode, HF) sits at the local frequency minimum (maximum). Black arrows represent the possible flow of magnons due to the finite mode volume of both B and HF. (d) Generation linewidth due to magnon-mediated scattering and inter-mode exchange mechanisms, by virtue of Eq. (2). Inset: magnon-scattering event between the dominant modes (ω_1 and ω_2) and thermal magnons.

the development of novel computation methods based on the interaction between magnetic solitons and propagating SWs¹⁹.

The paper is organized as follows: the multi-mode STO theory extended for coexistent modes with different frequencies is discussed in section II as well as the approximate Lorentzian linewidth expected from the generated dynamics. In section III, the physical origin of the mode coupling mechanisms in NC-STOs and their influence on the linewidth are discussed. The experiments and simulations performed to investigate the theoretical predictions are described in section IV. In section V, the experimental results are discussed and interpreted by means of the multi-mode STO theory predictions. Finally, we provide our conclusions in section VI.

II. MULTI-MODE THEORY FOR COEXISTING MODES: POWER AND LINEWIDTH

The magnetodynamics of NC-STOs can be described by means of the Landau-Lifshitz-Gilbert-Slonczewski

(LLGS) equation

$$\frac{d\hat{m}}{dt} = -\gamma\hat{m} \times \vec{H}_{eff} + \alpha\hat{m} \times \frac{d\hat{m}}{dt} - \gamma\mu_o\sigma(I)\epsilon\hat{m} \times (\hat{m} \times \hat{M}), \quad (1)$$

where $\gamma/2\pi = 28$ GHz/T is the gyromagnetic ratio, \hat{m} and \hat{M} are the normalized free and fixed layer magnetization vectors, respectively, α is the Gilbert damping, and $\sigma(I) = \hbar IP\lambda/\mu_o M_S eV$ is the dimensionless spin torque coefficient where \hbar is the reduced Planck constant, I is the spin-polarized current, P is the polarization, $\epsilon = \lambda/[1 + \lambda + (\lambda - 1)\hat{m} \cdot \hat{M}]$ is the spin asymmetry factor as a function of the spin torque asymmetry λ , μ_o is the vacuum permeability, M_S is the saturation magnetization, e is the electron charge, and V is the free layer volume. The effective field H_{eff} includes the exchange, demagnetizing, anisotropy, and external fields as well as the current-induced Oersted field. Throughout this paper, we will use the convention in which a negative current polarity opposes the damping and corresponds to electrons flowing from the free to the fixed layer.

Due to the nonlinearity of Eq. (1), analytical studies are usually performed by recasting the LLGS equation in a reduced basis^{29,30}. Such approaches assume a single-mode generation which is translated into a “winner-takes-all” strategy for the available energy resources³¹. The multi-mode theory of STOs^{25–28} differs in that it considers the existence of at least two excited modes. As a consequence, regimes of mode-hopping^{25,32}, periodic mode transitions³³, and coexistence¹¹ are obtained in addition to the single-mode regime.

The mode coexistence regime is of particular relevance due to its recent experimental observation¹¹ and the development of novel STO geometries^{20,21} that can potentially sustain multi-mode generation. In order to understand the features of this regime, it is important to relate the theory to experimental observables. The generation linewidth is one of the parameters that can be easily and accurately measured experimentally by straightforward electrical characterization. Consequently, we derive the generation linewidth predicted from the multi-mode STO theory for a coexistence regime for modes oscillating at generally different frequencies, ω_1 and ω_2 .

A simple approach is to assume that the phase difference between the modes is a linear function of time, equivalent to a constant “velocity”. Hence, it is possible to invoke Galilean invariance to generalize the equations of motion, as detailed in appendix A. We obtain a bounded phase space as a function of the energy and the phase difference ψ (in the “moving” frame) between the excited modes. In the theory, there is a linear coupling of amplitude K between the modes²⁵. In the case of strong mode coupling $K \gg \Gamma_p$, where Γ_p is the total restoration rate in STOs, the resulting phase space has stable fixed points solutions for $\psi = 2n\pi$, where n is an integer starting at 0, and equal energy share²⁸. This indicates that the coexistence regime is characterized by an equal split of the energetic resources in the system, in contrast to the single-mode scenario.

The generation linewidth can be obtained for each mode by computing the autocorrelation as a function of the time lag τ . Under Galilean invariance, the resulting autocorrelation function (appendix B) predicts identical linewidths for both modes. To first order in τ , the Lorentzian linewidth is given by

$$\Delta f_L \approx \Delta\omega_o \left(\frac{p_o^2 N^2 (\omega_1^{-1} - \omega_2^{-1})^2}{2(2\tilde{\alpha}K + 4K^2)} + 1 \right) \quad (2)$$

where p_o is the mode free-running power, $\Delta\omega_o \propto 1/p_o$ is the linear generation linewidth, N is the nonlinear frequency shift, $\tilde{\alpha} = (1 + a^2)/a$, and $a = \sqrt{\omega_1/\omega_2}$.

Equation 2 predicts that in this mode-coexistence regime the linewidth asymptotically decreases as a function of the coupling strength K . This result is in strong contrast to the mode-hopping regime²⁸ where the linewidth was predicted to increase as a function of K . It is noteworthy that these opposing trends suggest a smooth transition between the mode coexistence and mode-hopping regimes at an intermediate value of K . Consequently, Eq. (2) is only valid for mode coexistence and, as K approaches zero, mode-hopping [28] or single mode [e.g. Ref. 30] frameworks should be used instead.

III. MODE COUPLING MECHANISMS IN NC-STOS

In the previous section, we obtained the theoretical prediction of the linewidth behavior as a function of the coupling strength K ²⁷. The origin of this term has two important ingredients. The first one is the existence of a bath of thermally excited magnons that allows for on-the-shell scattering events that can couple two modes. Such a scattering event is schematically depicted in the inset of Fig. 1(d), where the two dominant modes with frequencies ω_1 and ω_2 can couple through a conservative four-magnon scattering event involving two thermal magnons with frequencies $\omega_{th,1}$ and $\omega_{th,2}$. The second is a non-local coupling between modes 1 and 2 mediated by magnetostatic interactions (we can safely assume that the speed of light c is infinite) or by exchange and magnetostatic coupling²⁷. By carefully controlling the experimental geometry and the applied current, these two interactions can be manipulated in different ways, giving rise to different experimental signatures. Firstly, through the STT and its pumping action, thermal magnons become easier to excite as a function of current, opening a growing number of scattering channels, and therefore increasing the coupling, between the two stable modes. By virtue of Eq. 2, this then leads to a linewidth decrease as a function of the bias current, as schematically shown by the solid black line in Fig. 1(d). We stress that the local Joule heating originating from electronic transport can also excite thermal magnon³⁴. However, for the investigated current range, such a temperature contribution is not expected to be a dominant effect.

Secondly, the mode coupling through the nonlocal interactions between the two dominant modes can be manipulated through the finite volume of the modes and the separation between them. In fact, the profile of the bullet mode was derived to be limited by the size of the NC⁸. In a coexistence regime, the NC must be sufficiently large to accommodate both the bullet and the high frequency mode, which is possible due to the preferential spatial location of each mode induced by the Oersted field [Fig. 1(a-c)]. Their mode volumes can overlap, leading to a coupling mediated by exchange. We will refer to this mechanism as inter-mode coupling. Clearly, the Oersted field plays a fundamental role in separating the modes and thus tuning the exchange and magnetostatic inter-mode coupling. This suggests the possibility to control the coupling by means of the bias current. Specifically, larger currents induce a stronger Oersted field which in turn will further spatially separate the modes¹¹ and reduce the inter-mode coupling strength. Invoking Eq. 2, the linewidth generated solely by this mechanism is expected to increase as a function of the bias current, as schematically shown by the solid red line in Fig. 1(d).

IV. DISENTANGLING MODE COUPLING MECHANISMS

The coupling mechanisms described above occur simultaneously in a NC-STO and have opposite effects on the generation linewidth, making it difficult to experimentally identify the expected features. However, considering the spatial dependence of the inter-mode coupling, it is possible to disentangle these mechanisms by breaking the symmetry at the nanoscale. This is achieved by fabricating NCs with an elliptical cross section.

The fabricated NC-STOs are based on a pseudo spin valve^{11,35} with the layer structure Co (8 nm)/Cu (8 nm)/Py (4.5 nm), where the Co (fixed layer) acts as a relatively static current spin-polarizer whereas the Py (Ni₈₀Fe₂₀, free layer) is subject to STT induced magnetodynamics. Devices with both circular NCs and elliptical NCs with an aspect ratio $r = 1.5$ are defined via electron beam lithography. A scanning electron microscopy (SEM) image of an elliptical NC with minor axis of 100 nm is shown in the inset of Fig. 2(a). Magnetization dynamics are excited by a dc current and electrically measured in a probe station featuring an external magnetic field set by a rotatable Halbach array of permanent magnets, creating a fixed and highly uniform field of $\mu_o H_a = 0.9$ T. The generated dynamics are separated from the dc current using a 0.1 – 40 GHz bias-T and converted to the frequency domain by a R&S FSV40 spectrum analyzer after using a 32 dB gain low-noise amplifier with a bandwidth of 18 – 40 GHz. In order to fine-tune and control the energy landscape, the elliptical NCs were patterned at different in-plane angles, ϕ_{NC} . In the measurement framework, such angles are measured

between the ellipses major axes and the in-plane field component $H_{\parallel} = H_a \sin(\theta)$, as schematically shown in the inset of Fig. 2(b). The fabricated devices have three different in-plane angles, namely $\phi_{NC} = 0, 45, \text{ and } 90^\circ$.

Representative spectra as a function of the external out-of-plane field angle, θ , are shown in Fig. 2(a) for an elliptical NC of minor axis 70 nm, rotated $\phi_{NC} = 0^\circ$, and biased at $I_{dc} = -18$ mA. Each spectrum was averaged 10 times with a video bandwidth of 10 kHz in order to minimize the noise. In agreement with our circular NC-STOs (not shown) and previous results^{8,10,11,36}, the spectra show a transition between the propagating spin wave mode predicted by Slonczewski⁵ and a mode-hopping regime. This transition occurs at a well-defined critical angle, θ_c , corresponding to the bullet mode onset^{10,36}. Additionally, we observe a second critical angle, θ_L , where both the bullet mode and a high frequency mode are observed, maintaining an approximately constant frequency difference¹¹.

The experimental spectra are well reproduced by micromagnetic simulations performed on the graphic-processing-unit-based code Mumax2³⁷. For the simulations, we assume standard parameters for the Py free layer and the spin polarization of the Co layer, namely: saturation magnetization $\mu_o M_s = 0.88$ T, exchange stiff-

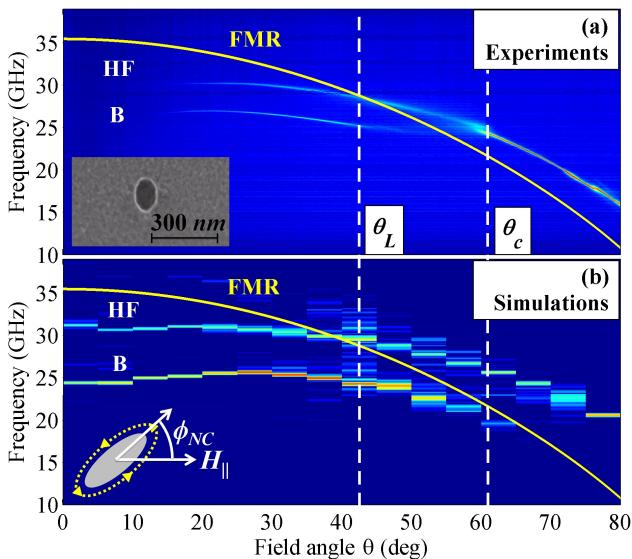


FIG. 2. (Color online) Field angle dependent spectra obtained (a) experimentally and (b) numerically using an elliptical NC with tilt $\phi_{NC} = 0^\circ$ and biased at -18 mA. The FMR frequency is shown by a yellow solid line. In both cases, the critical angle $\theta_c \approx 60^\circ$ defines the onset of mode-hopping regime which coincides with the onset of the bullet mode. A second critical angle $\theta_L \approx 42.5^\circ$ is also observed when both the bullet (B) and high frequency (HF) modes are localized, corresponding to a coexistence regime. The inset in (a) shows a SEM image of a fabricated elliptical contact with a minor axis of 100 nm. The inset in (b) schematically shows the convention of ϕ_{NC} with respect to the in-plane applied field H_{\parallel} .

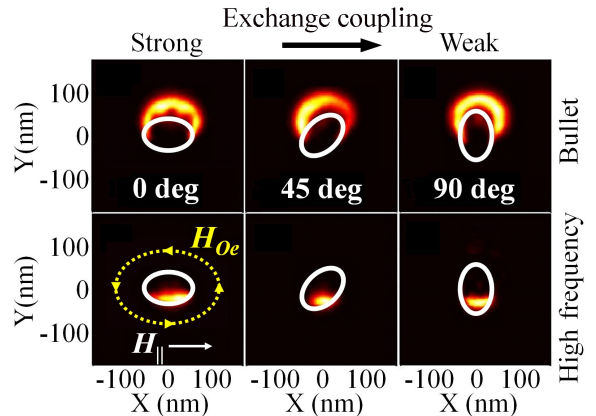


FIG. 3. (Color online) Mode energy distribution for the bullet and high frequency modes for NC-STOs with elliptical NCs tilted $\phi_{NC} = 0, 45, \text{ and } 90^\circ$. The relative orientations of the current-induced Oersted (yellow) and in-plane field component (white) are indicated in the lower left panel.

ness $A = 11$ pJ/m³, Gilbert damping $\alpha = 0.01$, spin polarization $P = 0.35$, and no out-of-plane torque as customary for pseudo spin valves with metallic spacers. The simulations shown here are performed using a symmetric torque $\lambda = 1$, although similar results are obtained with a more general antisymmetric torque, $\lambda > 1$. The tilt of the Co fixed layer is calculated for each external field angle θ by solving the magnetostatic boundary condition in a thin film approximation, considering a Co saturation magnetization of $\mu_o M_{s,p} = 1.5$ T. The simulated spectra, estimated from 10 ns long time traces [Fig. 2(b)], show excellent agreement with the experimental results. We stress that the frequency resolution is insufficient to accurately determine the power and linewidth from the simulated spectra. However, this is outside the scope of the present work as we determine such quantities experimentally.

The excellent spectral characteristics obtained from the micromagnetic simulations justify a closer inspection of the spatial energy distribution of the generated dynamics. In particular, we focus on the modes observed below $\theta_L \approx 42.5^\circ$. In Fig. 3, the spatial extent of the bullet (high frequency) mode for elliptical NCs tilted $0, 45, \text{ and } 90^\circ$ is observed to closely follow the edge of the NC (white), where the in-plane field component is minimal (maximal). Consequently, the elliptical NCs tilt allows us to control the strength of the inter-mode coupling mechanism, as indicated in Fig. 3. By virtue of the analytical predictions of section II, markedly different dependencies of the linewidth are expected for elliptical NCs tilted $\phi_{NC} = 0$ and 90° from the in-plane applied field.

V. EXPERIMENTAL RESULTS

To interpret the experimental results by means of the multi-mode STO theory, we must first determine the

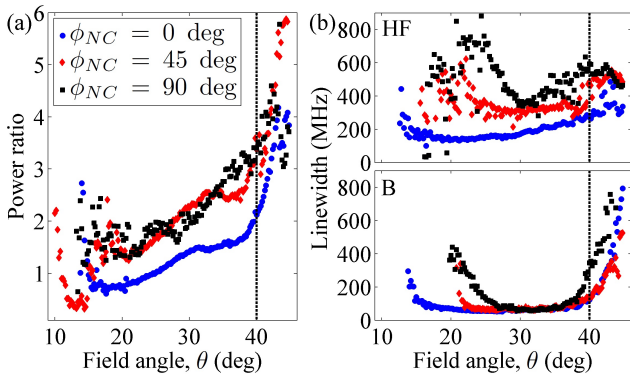


FIG. 4. (Color online) (a) Integrated power ratio between the high frequency and bullet mode, $p_{I,HF}/p_{I,B}$, for devices at $\phi_{NC} = 0$ (blue circles), 45 (red diamonds), and 90° (black squares), biased at currents between -16 to -26 mA. The modes have an integrated power ratio close to 1, denoting mode coexistence. Above $\theta = 40^\circ$ a divergence is observed, corresponding to the onset of a mode-hopping regime. (b) Linewidth of the high frequency (HF) and bullet (B) mode for a particular device biased at -18 mA. The HF mode exhibits variations between the devices with different ϕ_{NC} while the B mode remains mostly stable.

mode coexistence regime. In the frequency domain, indirect evidence of coexistence can be provided by a low frequency ($f < 2$ GHz) intermodulation feature¹¹. However, in our experiments, the bandwidth of the amplifier attenuates such low frequencies. Another approach is to confirm that the energy, or power, is approximately equally divided between the modes, as predicted by the fixed point solutions of the multi-mode STO theory^{27,28}. In our electrical measurements, this corresponds to an integrated power share between the modes. The integrated power, p_I , is directly extracted from the spectra by fitting Lorentzian lineshapes for each mode. Figure 4(a) shows the integrated power ratio between the high frequency and bullet mode, $p_{I,HF}/p_{I,B}$, as a function of field angle. The average values are obtained from elliptical NCs tilted 0 (blue circles), 45 (red diamonds), and 90° (black squares) biased at currents ranging from -16 to -26 mA. This average is possible to perform due to the similar current and field dependent characteristics of the fabricated devices. Clearly, the energy is best shared for the elliptical NC tilted $\phi_{NC} = 0^\circ$, suggesting a stronger coupling. For elliptical NCs tilted away from 0° , the ratio is larger although small enough to be still considered a coexistence regime. Note that the ratio diverges for $\theta > 40^\circ$ for all cases, corresponding to the transition between a coexistence regime and a mode-hopping dominated regime.

The corresponding generation linewidth of a particular set of devices as a function of applied field angle is shown in Fig. 4(b), also obtained from the Lorentzian fits. Here, we observe a markedly different behavior between the linewidth of the bullet mode and that of the high frequency mode. In particular, the bullet mode ex-

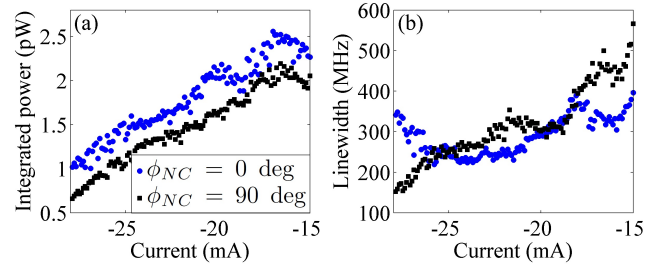


FIG. 5. (Color online) Integrated power (a) and linewidth (b) at $\theta = 30^\circ$ for devices with elliptical NCs satisfying $\phi_{NC} = 0$ (blue circles) and 90° (black squares). The data are obtained from averaging the results obtained from 5 nominally identical devices, exhibiting a similar threshold current of ≈ -15 mA. The integrated power in both cases decreases linearly in agreement with the Oersted field-induced mode separation. However, the linewidth exhibits different behaviors in correspondence with the mode coupling mechanisms in these devices. In particular, for $\phi = 90^\circ$, the magnon-mediated scattering mechanism dominates as observed from the average linewidth behavior.

hibits a much lower linewidth than the high frequency mode, whose minimum is nearly independent of ϕ_{NC} . Such a behavior can be understood from the schematic energy landscape shown in Fig. 1(c). The bullet mode is pinned at a local energy minimum, and is thus robust against fluctuations. On the other hand, the high frequency mode is perched upon a local energy maximum, an archetypal unstable condition, where it is more prone to fluctuations in frequency and thus to linewidth variations due to mode coupling. Consequently, the high frequency mode can be used as a probe for the aforementioned coupling mechanisms. For both the bullet and high frequency modes, the linewidth when $\theta > 40^\circ$ corresponds to the transition to a mode-hopping dominated regime.

We now investigate the mode coupling mechanisms and their influence on the generation linewidth of the high frequency mode. In order to directly relate the schematic representation of Fig. 1(d) to experiments, we perform current dependent measurements at a fixed out-of-plane field angle of $\theta = 30^\circ$. Figure 5(a-b) shows the high frequency mode integrated power and linewidth averaged from 5 devices with elliptical NCs at $\phi_{NC} = 0$ (blue circles) and 90° (black squares) and similar threshold current for auto-oscillations ≈ -15 mA. In Fig. 5(a), a linear decrease in integrated power is observed as a function of current magnitude. This is consistent with the Oersted-field induced inter-mode separation. In fact, as the modes move towards the boundaries of the NC, the current-carrying region cannot probe the entire magnetodynamics, leading to a reduced power^{11,24}. Within the theoretical framework described above, this observation provides direct evidence that the coexisting modes become increasingly more separated from one another as a function of current. Furthermore, the absolute value of the power is consistently smaller for the elliptical contact

tilted at 90° , suggesting an increased physical distance between the modes, as expected from the micromagnetic simulations shown in Fig. 3. This indicates that the inter-mode coupling mechanism when $\phi = 90^\circ$ is negligibly small compared to the magnon-mediated coupling.

The corresponding average linewidths [Fig. 5(b)] show two markedly different features. In the case of the elliptical NCs tilted at 0° (blue circles), the linewidth is bounded between 200 and 400 MHz, exhibiting a complex dependency that reflects the sample-to-sample variations and the competition between the two coupling mechanisms described above. On the other hand, the elliptical NCs tilted at 90° (black squares) exhibit a decrease in linewidth corresponding to the dependency expected from a purely magnon-mediated coupling. These observations provide direct proof of the mode coexistence regime and its relation to the dominant coupling mechanisms in these devices.

VI. CONCLUSIONS

NC-STOs were fabricated with elliptical NCs with the goal of breaking the symmetry of the system and fine-tune the energy landscape at the nanoscale. By electrically characterizing these devices, it was possible to find evidence of mode coexistence and the underlying coupling mechanisms by means of a multi-mode STO theory. The obtained results are consistent with two distinct coupling mechanisms, namely one dominated by magnons and the other dominated by inter-mode overlap. This study shows that the multi-mode STO theory is capable of predicting qualitatively the behavior of complex magnetodynamics, such as mode-hopping and mode coexistence. We expect this theory to be valuable in interpreting experimental results and to be extended to quantitatively describe the growing observations of multi-mode magnetodynamics. Furthermore, the ability to control the energy landscape and coupling mechanisms at the nanoscale is relevant for the development of magnonic applications based on the interaction between solitonic modes and propagating spin waves.

ACKNOWLEDGEMENTS

This work was supported by the European Commission FP7-ICT-2011-contract No. 317950 ‘‘MOSAIC’’. The work by O.H. was funded by the Department of Energy Office of Science, Materials Sciences and Engineering Division. Support from the Swedish Research Council (VR), the Swedish Foundation for Strategic Research (SSF), and the Knut and Alice Wallenberg Foundation is gratefully acknowledged.

APPENDIX

Appendix A: Auto-oscillator complex amplitude under Galilean invariance

The dynamics of a nonlinear auto-oscillator can be represented by its complex amplitude³⁰

$$c = \sqrt{p}e^{i\phi}, \quad (\text{A1})$$

where p and ϕ are the (generally time-dependent) power and phase. Furthermore, it is possible to cast the phase as $\phi = \omega t + \phi_0$, for a well defined oscillation frequency ω .

In the case of two coupled oscillators, we can write the phase difference and addition as $\varphi = \phi_2 - \phi_1 = \Delta\omega t + \varphi_0$ and $\Psi = \phi_2 + \phi_1 = \Omega t + \Psi_0$, where $\Delta\omega = \omega_2 - \omega_1$ and $\Omega = \omega_2 + \omega_1$. Without loss of generality, we can set $\varphi_0 = \Psi_0 = 0$. For the coupling regimes discussed in the main text and Ref. 28, the phases of the oscillators are perturbed, leading to $\varphi = \Delta\omega t + \delta\varphi$ and $\Psi = \Omega t + \delta\varphi$. Here, we will assume that $\Omega t \gg \delta\varphi$ and that the reference frame of the coupled system is established by the well defined frequency difference $\Delta\omega$. In other words, we establish that the phase difference fluctuations $\delta\varphi$ are solved under Galilean invariance. Finally, the complex amplitudes for the coupled oscillators are

$$c_1 = \sqrt{p_1}e^{i(\Omega t - \Delta\omega t - \delta\varphi)/2}, \quad (\text{A2a})$$

$$c_2 = \sqrt{p_2}e^{i(\Omega t + \Delta\omega t + \delta\varphi)/2}. \quad (\text{A2b})$$

Appendix B: Autocorrelation for coexistent modes

The autocorrelation function of the coupled auto-oscillators,

$$\mathcal{K} = \langle [c_1(t) + c_2(t)], [c_1^*(t') + c_2^*(t')] \rangle \quad (\text{B1})$$

provides the required information to determine the generation linewidth. Solving Eq. (B1) by using the definitions of Eq. (A2), we obtain

$$\begin{aligned} \mathcal{K} &= p_1 e^{i\omega_1 t} e^{-\langle \delta\varphi(t), \delta\varphi(t') \rangle / 2} \\ &= p_2 e^{i\omega_2 t} e^{-\langle \delta\varphi(t), \delta\varphi(t') \rangle / 2}. \end{aligned} \quad (\text{B2})$$

The most interesting feature of Eq. (B2) is the fact that the phase autocorrelation is identical for both modes, indicating an identical linewidth.

To obtain the linewidth, it is possible to follow the same method introduced in Ref. 28 where the coupled power and phase equations are linearized and solved by standard matrix algebra. Further assuming that in the case of coexistence the power is equally split and $\langle \varphi - \Delta\omega t \rangle = 0$, we are left with

$$\begin{aligned} \langle \delta\varphi(t), \delta\varphi(t') \rangle &= \frac{\Delta\omega_o}{K\beta} \\ &\times \left(\frac{p_o^2 C^2}{(P + K\alpha)^2 - (K\beta)^2} + 2 \right) e^{K\beta\tau}, \end{aligned} \quad (\text{B3})$$

where $\Delta\omega_o$ is the linear linewidth for STOs, K is the coupling strength, $C = -N/2(\omega_2^{-1} - \omega_1^{-1})$, N is the nonlinear frequency shift, P is a term proportional to the STO bias, $\alpha = (1 + a^2)/a$, $\beta = (1 - a^2)/a$, $a = \sqrt{\omega_1/\omega_2}$, and $\tau = |t - t'|$ is the time lag. Expanding the exponential of Eq. (B3) to first order, we obtain the Lorentzian contribution to the linewidth, cast in Eq. (2). As for the

case of mode-hopping, a Gaussian contribution is also present by expanding the exponential to second order. However, we are interested here in the qualitative behavior of the linewidth with coupling strength K , so that Lorentzian fits are sufficient to study the behavior of the experimentally measured spectra.

-
- ¹ T. Silva and W. Rippard, *Journal of Magnetism and Magnetic Materials* **320**, 1260 (2008).
- ² D. Ralph and M. Stiles, *Journal of Magnetism and Magnetic Materials* **320**, 1190 (2008).
- ³ J. C. Slonczewski, *Journal of Magnetism and Magnetic Materials* **159**, L1 (1996).
- ⁴ L. Berger, *Phys. Rev. B* **54**, 9353 (1996).
- ⁵ J. C. Slonczewski, *Journal of Magnetism and Magnetic Materials* **195**, 261 (1999).
- ⁶ M. R. Pufall, W. H. Rippard, S. E. Russek, S. Kaka, and J. A. Katine, *Phys. Rev. Lett.* **97**, 087206 (2006).
- ⁷ M. Madami, S. Bonetti, G. Consolo, S. Tacchi, G. Carlotti, G. Gubbiotti, F. B. Mancoff, M. A. Yar, and J. Åkerman, *Nature Nanotechnology* **6**, 635 (2011).
- ⁸ A. Slavin and V. Tiberkevich, *Phys. Rev. Lett.* **95**, 237201 (2005).
- ⁹ V. E. Demidov, S. Urazhdin, and S. O. Demokritov, *Nature Materials* **9**, 984 (2010).
- ¹⁰ S. Bonetti, V. Tiberkevich, G. Consolo, G. Finocchio, P. Muduli, F. Mancoff, A. Slavin, and J. Åkerman, *Phys. Rev. Lett.* **105**, 217204 (2010).
- ¹¹ R. K. Dumas, E. Iacocca, S. Bonetti, S. R. Sani, S. M. Mohseni, A. Eklund, J. Persson, O. Heinonen, and J. Åkerman, *Phys. Rev. Lett.* **110**, 257202 (2013).
- ¹² V. Pribiag, I. N. Krivorotov, G. D. Fuchs, P. M. Braganca, O. Ozatay, J. C. Sankey, D. C. Ralph, and R. A. Buhrman, *Nature Physics* **3**, 489 (2007).
- ¹³ T. Devolder, J.-V. Kim, M. Manfrini, W. van Roy, L. Lagae, and C. Chappert, *Applied Physics Letters* **97**, 072512 (2010).
- ¹⁴ M. A. Hoefer, T. J. Silva, and M. W. Keller, *Phys. Rev. B* **82**, 054432 (2010).
- ¹⁵ S. M. Mohseni, S. R. Sani, J. Persson, T. N. A. Nguyen, S. Chung, Y. Pogoryelov, P. K. Muduli, E. Iacocca, A. Eklund, R. K. Dumas, S. Bonetti, A. Deac, M. A. Hoefer, and J. Åkerman, *Science* **339**, 1295 (2013).
- ¹⁶ E. Iacocca, R. K. Dumas, L. Bookman, M. Mohseni, S. Chung, M. A. Hoefer, and J. Åkerman, *Phys. Rev. Lett.* **112**, 047201 (2014).
- ¹⁷ Y. Zhou, E. Iacocca, A. Awad, R. Dumas, H. Zhang, H. B. Braun, and J. Åkerman, arXiv:1404.3281v2 (2014).
- ¹⁸ S. Bonetti and J. Åkerman, in *Magnonics*, Topics in Applied Physics, Vol. 125, edited by S. O. Demokritov and A. N. Slavin (Springer Berlin Heidelberg, 2013) pp. 177–187.
- ¹⁹ N. Locatelli, V. Cros, and J. Grollier, *Nature Materials* **13**, 11 (2013).
- ²⁰ V. Demidov, S. Urazhdin, H. Ulrichs, V. Tiberkevich, A. Slavin, D. Baither, G. Schmitz, and S. Demokritov, *Nature Materials* **11**, 1028 (2012).
- ²¹ M. Ranjbar, P. Dürrenfeld, M. Haidar, E. Iacocca, M. Balinskiy, T. Le, M. Fazlali, A. Houshang, A. Awad, R. Dumas, and J. Åkerman, *Magnetics Letters, IEEE* **5**, 3000504 (2014).
- ²² J. E. Hirsch, *Phys. Rev. Lett.* **83**, 1834 (1999).
- ²³ M. A. Hoefer, T. J. Silva, and M. D. Stiles, *Phys. Rev. B* **77**, 144401 (2008).
- ²⁴ G. Consolo, G. Finocchio, G. Siracusano, S. Bonetti, A. Eklund, J. Åkerman, and B. Azzerboni, *Journal of Applied Physics* **114**, 153906 (2013).
- ²⁵ P. K. Muduli, O. G. Heinonen, and J. Åkerman, *Phys. Rev. Lett.* **108**, 207203 (2012).
- ²⁶ O. Heinonen, P. Muduli, E. Iacocca, and J. Åkerman, *Magnetics, IEEE Transactions on* **49**, 4398 (2013).
- ²⁷ O. Heinonen, Y. Zhou, and D. Li, arXiv:1310.6791 (2013).
- ²⁸ E. Iacocca, O. Heinonen, P. K. Muduli, and J. Åkerman, *Phys. Rev. B* **89**, 054402 (2014).
- ²⁹ S. M. Rezende, F. M. de Aguiar, and A. Azevedo, *Phys. Rev. Lett.* **94**, 037202 (2005).
- ³⁰ A. Slavin and V. Tiberkevich, *Magnetics, IEEE Transactions on* **45**, 1875 (2009).
- ³¹ F. M. de Aguiar, A. Azevedo, and S. M. Rezende, *Phys. Rev. B* **75**, 132404 (2007).
- ³² P. K. Muduli, O. G. Heinonen, and J. Åkerman, *Phys. Rev. B* **86**, 174408 (2012).
- ³³ S. Bonetti, V. Puliafito, G. Consolo, V. S. Tiberkevich, A. N. Slavin, and J. Åkerman, *Phys. Rev. B* **85**, 174427 (2012).
- ³⁴ S. Petit-Watelot, R. M. Otxoa, M. Manfrini, W. Van Roy, L. Lagae, J.-V. Kim, and T. Devolder, *Phys. Rev. Lett.* **109**, 267205 (2012).
- ³⁵ S. Sani, J. Persson, S. Mohseni, Y. Pogoryelov, P. K. Muduli, A. Eklund, G. Malm, M. Käll, A. Dmitriev, and J. Åkerman, *Nature Comm.* **4**, 2731 (2013).
- ³⁶ G. Gerhart, E. Bankowski, G. A. Melkov, V. S. Tiberkevich, and A. N. Slavin, *Phys. Rev. B* **76**, 024437 (2007).
- ³⁷ A. Vansteenkiste and B. V. de Wiele, *Journal of Magnetism and Magnetic Materials* **323**, 2585 (2011).